



HAL
open science

Impact of stresses and restraints on ASR expansion

Pierre Morenon, Stéphane Multon, Alain Sellier, Etienne Grimal, Francois Hamon, Eric Bourdarot

► **To cite this version:**

Pierre Morenon, Stéphane Multon, Alain Sellier, Etienne Grimal, Francois Hamon, et al.. Impact of stresses and restraints on ASR expansion. *Construction and Building Materials*, 2017, 140, pp.58–74. 10.1016/j.conbuildmat.2017.02.067 . hal-01724648

HAL Id: hal-01724648

<https://insa-toulouse.hal.science/hal-01724648v1>

Submitted on 20 Feb 2019

HAL is a multi-disciplinary open access archive for the deposit and dissemination of scientific research documents, whether they are published or not. The documents may come from teaching and research institutions in France or abroad, or from public or private research centers.

L'archive ouverte pluridisciplinaire **HAL**, est destinée au dépôt et à la diffusion de documents scientifiques de niveau recherche, publiés ou non, émanant des établissements d'enseignement et de recherche français ou étrangers, des laboratoires publics ou privés.

IMPACT OF STRESSES AND RESTRAINTS ON ASR EXPANSION

Pierre Morenon^{1,2*}, Stéphane Multon², Alain Sellier², Etienne Grimal¹, François Hamon³, Eric Bourdarot¹

¹Electricité de France, Centre d'Ingénierie Hydraulique, EDF-CIH Technolac, 73373 Le Bourget du Lac Cedex France

²LMDC, Université de Toulouse, INSA/UPS Génie Civil, 135 Avenue de Rangueil, 31077 Toulouse cedex 04 France

³EDF Lab Paris – Saclay, 7 boulevard Gaspard Monge Bureau 02-B07 91120 Palaiseau - France

Abstract

Some large civil engineering structures, principally certain concrete dams, are subject to the structural effects of Alkali-Silica Reaction (ASR). Due to the directions of loading and reinforcement, the stress state is mostly anisotropic. The aim of this paper is to describe the impact of applied stresses and restraint due to reinforcement or boundary conditions on ASR-expansion and induced anisotropic cracking. After the definition and validation of the poromechanical modelling, the paper gives a detailed description of the effects of different aspects of stress (in one, two or three directions) and reinforcement on ASR-expansion for engineers in charge of damaged structures.

Keywords: Alkali-Silica Reaction, concrete modelling, stresses effects, anisotropy, damage

Highlights:

Impacts of applied stresses and restraints on ASR-expansion are compared.

The anisotropy of expansion is induced by the resolution of the mechanical equilibrium between stresses and the isotropic pressure of ASR-gel using a cracking criterion.

* Corresponding author. E-mail address: morenon@insa-toulouse.fr (P. Morenon). LMDC, Université de Toulouse, INSA/UPS Génie Civil, 135 Avenue de Rangueil, 31077 Toulouse cedex 04 France

Tel.: +33 5 61 55 99 16 - Fax. : +33 5 61 55 99 49.

23 The model is calibrated and validated on experimental results under multi-axial loading and restraints.
24 Theoretical tests were conducted in order to analyse the model response (strains, stresses and gel
25 pressure) under several kinds of loading (multi-axial compression, unloading and tension).
26 Reinforcement induces concrete prestress and anisotropic cracking.

27 **1. Introduction**

28 Alkali-silica reaction (ASR) occurs on structures that contain some specific siliceous reactive
29 aggregates. Engineers discovered this pathology through the observation of cracking on basements.
30 Among large civil engineering structures, concrete dams, in particular, are subject to structural effects
31 caused by ASR [1–4]. This is mainly attributable to the concrete composition and climatic conditions
32 such as water supply. These swellings can lead to damage and cracks on structures and result in a
33 decrease of their stability.

34 The main aim for dam owners is to ensure the safety of the population while optimizing
35 maintenance. Many authors are working on ASR modelling in order to predict the long-term
36 behaviour of affected structures [5–9]. Relevant modelling can also anticipate the choice of options
37 during repairs.

38 ASR expansion occurs in structures that sustain significant loads, such as bridge piers, or are
39 restrained by external loading conditions, such as dams in valleys. Restraining expansion by
40 reinforcement and prestressing in structures also causes stresses during expansion. In order to manage
41 the damaged structures, owners need reliable tools to predict future damage. Stress free ASR swelling
42 has been largely studied and several models reproduce the phenomenon realistically. Despite the
43 number of experiments, ASR swelling under restraint is not yet fully understood and modelled.

44 The aim of the present paper is to describe the impact of applied stresses and stresses induced
45 by restraints due to reinforcement or boundary conditions on ASR-expansion and anisotropic cracking.
46 In the model, the anisotropy of expansion is not introduced through chemical loading with empirical
47 relationships but by the resolution of the mechanical equilibrium between stresses (due to external

48 loading, prestressing, or restraint and boundary conditions) and the isotropic pressure of ASR-gel,
49 through a cracking criterion assessed in the three main directions. An anisotropic stress state will
50 induce anisotropic cracking and, as a result, anisotropic expansion. After a description of the model,
51 parameters are fitted and validated on multi-axial restrained experiments drawn from the literature
52 [10]. Based on this calibration, a parametric study is conducted to assess the multi-axial behaviour of
53 affected concrete in various loading and unloading conditions. Then, tests are performed on steel bars
54 and rings embedded in concrete cylinders in order to assess the impact of usual reinforcement on
55 anisotropy swelling. Maximum stresses and damage are observed with particular attention in all tests
56 to obtain practical considerations useful for engineering. This study shows what impact of stresses can
57 be expected in restrained and in reinforced or prestressed structures subjected to ASR expansion. It
58 also highlights the risks of misanalysing experimental results obtained on cores drilled from structures.

59 **2. Constitutive equations**

60 *2.1. Rheological model*

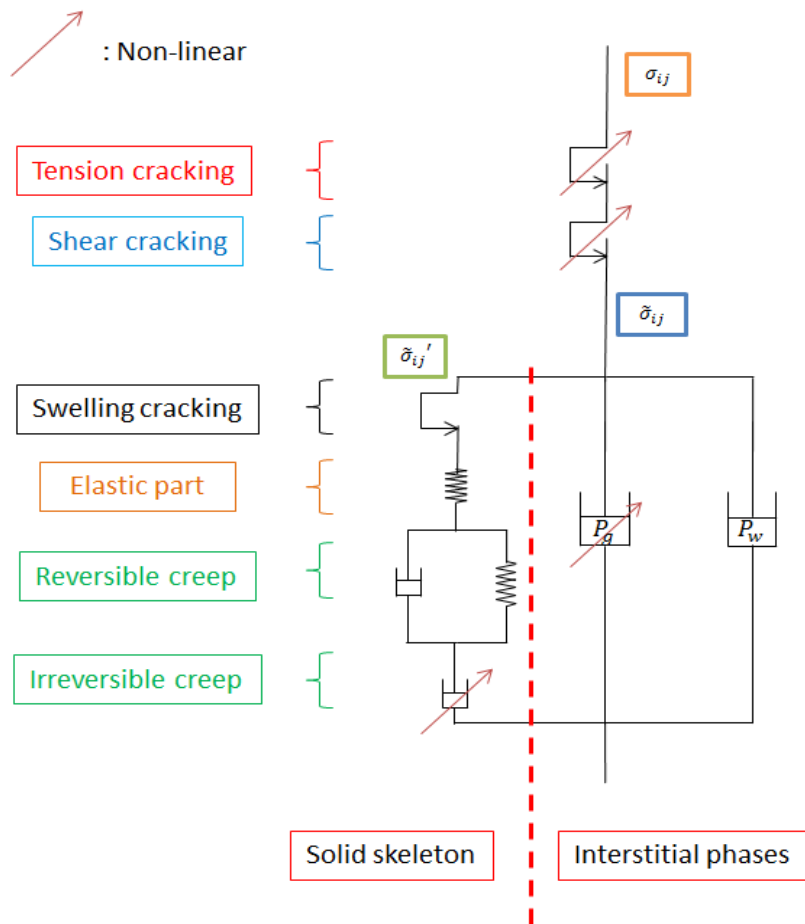
61 In this work, the concrete behaviour is modelled in the poro-mechanical framework. The
62 model comprises a damage model (inspired from [11]), and a rheological model [12], in order to
63 consider realistic interactions between ASR, creep, shrinkage and damage so as to reproduce the
64 mechanical effects occurring in real structures.

65 Concrete cracking is described by a non-linear model using anisotropic plastic criteria and
66 damage [11]. The model has recently been improved to calculate plastic strains. Two groups of criteria
67 have been added (Fig. 1): one to manage shear cracking (Drucker Prager criteria), which is an
68 isotropic scalar, and one to represent tension behaviour (Rankine criteria), which is an orthotropic
69 tensor. Shear cracking is used to reproduce concrete behaviour in compression [11]. The tension
70 criterion separates structural macro-cracks, reclosing macro-cracks (tension cracking in Fig. 1) and
71 intra-porous pressure micro-cracks (ASR) by considering the gel pressure P_g .

72 The creep model, a Burger chain (Fig. 1), has been clarified and implemented in a poro-plastic
73 framework [12]. Reversible creep is modelled with a Kelvin-Voigt floor and the Maxwell module

74 (irreversible creep) uses an anisotropic formulation of the viscous strains in order to reproduce multi-
 75 axial consolidation of the material. Concrete shrinkage can also be taken into account through the
 76 water pressure P_w thanks to the poro-mechanical framework (Fig. 1).

77 The total stress is calculated by using the damage and the effective stress (1). The latter is
 78 obtained by considering the difference between the effects of gel and water on the solid skeleton (Fig.
 79 1 and (2)). In the poromechanical framework, gel pressure, P_g , and water pressure, P_w , are impacted by
 80 Biot coefficients [13], respectively b_g and b_w , for the ASR-gel pressures and the water pressure
 81 inducing shrinkage. The effective poromechanical stress increment $\tilde{\sigma}_{ij}'$ is calculated from the stiffness
 82 matrix S_0 and the elastic strain obtained from the total strain increment $\dot{\epsilon}$, the plastic increment $\dot{\epsilon}_{pl}$, the
 83 creep increment $\dot{\epsilon}_{cr}$ and the thermal increment $\dot{\epsilon}_{th}$ (3).



84

85

Fig. 1. Rheological scheme of the model.

$$\sigma_{ij} = (1 - D)\tilde{\sigma}_{ij} \quad (1)$$

86

$$\tilde{\sigma}_{ij} = \tilde{\sigma}_{ij}' - b_g P_g - b_w P_w \quad (2)$$

87

$$\tilde{\sigma}_{ij}' = S_0 (\dot{\varepsilon} - \dot{\varepsilon}_{pl} - \dot{\varepsilon}_{cr} - \dot{\varepsilon}_{th}) \quad (3)$$

88 This paper focuses on ASR modelling, including ASR pressure and kinetics and their links to
 89 anisotropic cracking. The other aspects of the model, such as the formulation of the visco-plastic creep
 90 model, are detailed in [12], independently of the new developments reported below.

91 2.2. ASR model

92 2.2.1. Chemical advancement

93 ASR advancement A^{asr} varies from 0 (before the start of the reaction) to 1 (when the reaction
 94 ends). Its evolution principally depends on the temperature and the humidity of the material (4). The
 95 chemical advancement must be determined in order to evaluate the evolution of ASR-gel pressure. It
 96 depends on the characteristic time of the reaction τ_{ref}^{asr} (a material parameter), the temperature
 97 coefficient $C^{T,asr}$, the humidity coefficient $C^{W,asr}$, the maximum value of the advancement $A^{asr \infty}$
 98 and the advancement itself A^{asr} .

99 The effect of temperature on advancement $C^{T,asr}$ is managed by an Arrhenius law (5). Two
 100 material parameters define the impact of temperature: the activation energy for ASR kinetic E^{asr} (\approx
 101 40,000 J/Mol [14]) and the reference temperature T_{ref} for which τ_{ref}^{asr} was set.

102 The effect of humidity on advancement, $C^{W,asr}$, is described through a power law (6). S_r
 103 represents the saturation degree and $S_r^{th,asr}$ the humidity threshold below which the reaction stops.
 104 When the material is not saturated, the reaction kinetics slows down - and it stops totally in very dry
 105 concrete.

106 Finally only four material parameters are used to manage ASR advancement according to
 107 environmental conditions: τ_{ref}^{asr} (characteristic time of AAR), $S_r^{th,asr}$ (water saturation rate minimum
 108 threshold), E^{asr} (activation energy for AAR kinetics) and T_{ref} (reference temperature of τ_{ref}^{asr} fitting).

$$\frac{\delta A^{asr}}{\delta t} = \frac{1}{\tau_{ref}^{asr}} C^{T,asr} C^{W,asr} (A^{asr \infty} - A^{asr}) \quad (4)$$

109

$$C^{T,asr} = \exp\left(-\frac{E^{asr}}{R}\left(\frac{1}{T} - \frac{1}{T_{ref}}\right)\right) \quad (5)$$

110

$$C^{W,asr} = \begin{cases} \left(\frac{S_r - S_r^{th,asr}}{1 - S_r^{th,asr}}\right)^2 & \text{if } S_r > S_r^{th,asr} \\ 0 & \text{if } S_r \leq S_r^{th,asr} \end{cases} \quad (6)$$

111 2.2.2. Gel pressure

112 The fraction of gel produced by the reaction per m^3 of concrete is ϕ_g . It is the product of the
 113 advancement A^{asr} and the maximum gel potential ϕ_g^∞ , which is a characteristic of the material (7).

$$\phi_g = \phi_g^\infty \cdot A^{asr} \quad (7)$$

114

115 Gel exerts a pressure P_g (8) on aggregate and concrete. In this model, a macroscopic approach
 116 is used and P_g is the average pressure assumed to be transferred by the aggregate to the concrete. It
 117 mainly depends on the accessible porosity, the initial porosity or that created by strains (elastic or
 118 plastic).

$$P_g = M_g \left(\phi_g - \left(\phi_g^v \left(\frac{P_g}{\tilde{R}_I^t} \right) + b_g \text{tr}(\varepsilon^e + \varepsilon^{cr}) + \text{tr}(\varepsilon^{p,g}) \right) \right) \quad (8)$$

119

120 ϕ_g^v is the fraction of gel not effective in creating expansion under characteristic pressure fixed at the
 121 effective tensile strength \tilde{R}_I^t (gel that is non-swelling for chemical reasons, or gel migrating to
 122 available porosity). For a specimen in free swelling conditions, when the gel pressure P_g reaches \tilde{R}_I^t ,
 123 micro-cracking of the concrete element begins. In cases of constrained swelling, the pressure needed

124 to start cracking rises because it is partially balanced by the external stress as explained below. Then,
 125 the gel amount (which migrates into the connected porosity of the concrete) increases. It leads to
 126 delayed, anisotropic cracking. The management of these aspects will be clarified in the section related
 127 to the modelling of ASR cracking.

128 M_g is the gel Biot modulus, which is obtained from a poromechanical definition (9). Φ is the initial
 129 porosity. K_s is the skeleton bulk modulus defined by the Young's Modulus and the Poisson coefficient
 130 (10). b_g is the Biot coefficient, which is obtained from poromechanical considerations [13].

$$\frac{1}{M_g} = \frac{\Phi - b_g}{K_s} + \frac{b_g}{K_g} \quad (9)$$

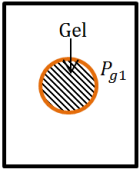
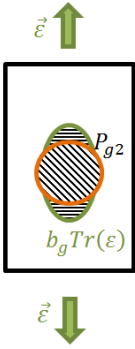

$$K_s = \frac{E}{3(1 - 2\nu)} \quad (10)$$

131 Several authors have tried to measure the gel bulk modulus K_g (9) or the gel Young's Modulus
 132 E_g . Table 1 summarizes these results and proposes a corresponding Gel Biot modulus M_g obtained
 133 from equations (9) and (10). Here, M_g is equal to 27.7 GPa, which leads to K_g equal to 4.8 GPa (more
 134 than twice the modulus of water).

	Author(s)	Accessible data	M_g calculated (Equations 10 and 11)
Experimental	[15]	K_g from 24.9 to 34 GPa	From 90 to 110 GPa
	[16] [17]	E_g from 7 to 45 GPa, $0.16 < \nu < 0.22$	From 20 to 80 GPa
	[18]	K_g equals 2.2 GPa (close to the water bulk modulus)	13.5 GPa
Modelling values	[19]	-	21.7 GPa
	[7]	-	27.7 GPa

135 Table 1. Gel Biot modulus M_g from the literature.

136 In the modelling, the gel pressure P_g (8) is managed by two main parts. The first one is the
 137 non-effective gel volume, $\phi_g^v \left(\frac{P_g}{\tilde{R}_I^t} \right)$. When $P_g > \tilde{R}_I^t$ (triaxial restraint for example), the gel spreads over
 138 the connected porosity under pressure and little expansion is observed on all ASR expansion curves.
 139 The second part of the expression is the volume $b_g tr(\epsilon^e + \epsilon^{cr})$, which represents the porosity created
 140 by elastic and creep strains and that absorbs a part of the gel without creating pressure. The entire
 141 volume created by strains (except the ASR plastic volume, which represents the volume of cracks due
 142 to ASR) is multiplied by the Biot coefficient b_g , which comes from poromechanical considerations
 143 [13] as $b_g tr(\epsilon)$ represents the variation of the porosity volume filled by ASR-gel under concrete
 144 strain. Grimal's model [7,11] gives a calibration of b_g lying between 0.1 and 0.4. For the volume of
 145 cracks induced by ASR (and represented by plastic strains $\epsilon^{p,g}$ in this model), b_g equals 1 because
 146 cracks created by the gel are assumed to be always totally accessible for the gel, here, and thus
 147 completely filled (Table 2).

Free swelling	Swelling under structural strain	Swelling under structural strain and ASR micro-cracking
		

For $A^{aar} = \text{constant}$, $P_{g1} > P_{g2} > P_{g3}$

148 Table 2. Strain effects on gel pressure. $b_g tr(\epsilon)$ is the variation of the porosity due to concrete strain.
 149 $tr(\epsilon^{p,g})$ is the variation of the porosity due to plastic ASR-cracking (taken to be plastic strains in this
 150 model).

151 To conclude this part on gel pressure, four parameters have to be fitted on the model: the
 152 maximum gel potential, ϕ_g^∞ ; the fraction of non-effective gel, ϕ_g^v ; the stress concentration factor, k_g ;
 153 and the Biot coefficient, b_g .

154 2.2.3. Modelling of ASR cracking

155 In this model, the cracks created by ASR are represented by plastic strains. When specimens
 156 are subjected to drying shrinkage after ASR expansion, the shrinkage strains are the same as for
 157 specimens without ASR before drying [20]. During shrinkage, the strains are not modified by the

158 previous expansions, which can thus be represented by irreversible plastic strains. The swelling
 159 difference between aggregates and paste induces a shift between lips, which leads to irreversible
 160 plastic strains even when the pressure changes in ASR-gels.

161 P_g is used to determine micro-cracking due to ASR by a special criterion f_I^g , which takes the
 162 stress state into account (11). $\tilde{\sigma}_I$ is the principal tensile stress in direction I.

$$\begin{cases} f_I^g = P_g & \text{if } \tilde{\sigma}_I \geq \tilde{R}_I^t \\ f_I^g = P_g + \tilde{\sigma}_I - \tilde{R}_I^t & \text{if } \tilde{\sigma}_I < \tilde{R}_I^t \end{cases} \text{ with } I \in [\text{I,II,III}] \quad (11)$$

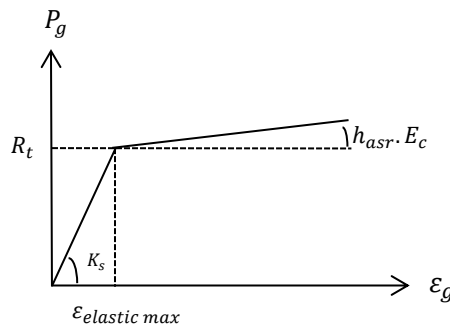
163 The hardening law that links ASR pressure to ASR strain can be drawn with a bilinear curve
 164 (Fig. 2). K_s represents the bulk modulus, E_c represents the concrete Young's modulus and h_{asr} the
 165 plastic hardening ratio ($h_{asr} \cdot E_c$ is the hardening modulus). h_{asr} is less than 0.05 and may be
 166 determined by analysing the results of low stress state experiments. These results come from the
 167 analysis of beams studied by Multon et al. [20].

168 During free swelling, when the gel pressure reaches R_t , ASR induces the creation of micro-
 169 cracks that are filled by the gel. The corresponding strains are modelled using plastic strains. A
 170 coefficient h_{asr} close to 0 means that, when R_t is reached, plastic ASR strains rise very quickly with
 171 a slight increase of pressure (as P_g is proportional to h_{asr}). If h_{asr} is not zero, the evolution of ASR
 172 plastic strains is possible only if the gel pressure increases, and the micro-cracking induced by the gel
 173 is stable.

174 This quantification of the micro-cracking also expresses the fact that ASR-cracks do not
 175 appear for exactly the same advancement in all aggregates in stress free conditions. In reality,
 176 heterogeneity of ASR-cracking can be observed due to variations of tensile strength in the concrete,
 177 which lead to progressive cracking with increasing gel pressure. The plastic hardening law provides a
 178 good simplified representation of this phenomenon.

179 In free swelling tests, the plastic criterion (11) is reached in all directions at the same time and
 180 cracks appear in all directions (Fig. 3). However, once specimens are loaded, cracking is oriented

181 perpendicularly to the loading direction (Fig. 3). The anisotropy of cracking leads to the expansion
 182 anisotropy that is usually observed. This is obtained by Eq. (11 in the model, in which compressive
 183 stress delays cracking (while tensile stress can accelerate it) in the loading direction. With Eq. (11,
 184 when a compression stress is applied to concrete ($\sigma < 0$), cracking first appears in a direction
 185 perpendicular to the loading (directions II and II in Fig. 3). Then, P_g increases, depending on the value
 186 of h_{asr} . If $\tilde{R}_I^g - \sigma$ can also be reached in the loaded direction, cracking can also be initialized
 187 perpendicular to this direction (major principal direction in Fig. 3).



188

Fig. 2: Plastic ASR hardening law

189

190 Kagimoto et al. [21] cast a beam with external steel beams to restrain displacement. The crack
 191 pattern (Fig. 4) shows a usual main cracking direction (the direction of the steel bars). However, one
 192 crack is perpendicular to the main cracks. In reinforced structures, stress is induced by the gel pressure
 193 itself and P_g increases slowly. The ASR plastic criterion is the first to be reached because $\tilde{\sigma}_1 (= b_g P_g)$
 194 is smaller than $P_g (= \tilde{R}^t)$ with $b_g < 1$. The material is in compression but not enough to prevent
 195 cracks from occurring, so it can crack due to gel pressure perpendicular to the reinforcement. Larive
 196 [14] applied external compression stress to a sample but the applied stresses (5 and 10 MPa) seem to
 197 have been too high for cracks to be observed perpendicular to the applied stress direction.

198 Numerically, swelling is evaluated through $Tr(\varepsilon_{pl}^g + \varepsilon_{creep}^g)$ (which expresses the plastic strains
 199 (cracking) and the creep strains induced by the gel), and through the elastic strain induced by ASR
 200 swelling (12).

$$Volumic\ ASR\ strain = Tr(\varepsilon_{pl}^g + \varepsilon_{creep}^g) + \frac{b_g P_g}{\left(\frac{E}{3(1-2\nu)}\right)} \quad (12)$$

201 2.2.4. ASR anisotropic damage

202 ASR damage is anisotropic. It is calculated from ASR plastic strains $\varepsilon_I^{pl,ISR}$ and a material
 203 parameter to calibrate damage kinetics $\varepsilon^{k,ISR}$ (13).

$$D_I^{t,ISR} = \frac{\varepsilon_I^{pl,ISR}}{\varepsilon_I^{pl,ISR} + \varepsilon^{k,ISR}} \quad (13)$$

204 $\varepsilon^{k,ISR}$ has been calibrated to approximately 0.3% [22]. The damage matrix due to ASR is a diagonal
 205 matrix which principal directions are $\varepsilon_{I,II,III}^{pl,ISR}$.

206

207 The ASR compression damage matrix is obtained from the ASR tension damage matrix (14).
 208 ASR tension damage in principal directions *II* and *III* has an impact on ASR compression damage in
 209 principal direction *I*. Furthermore, when three orthogonal cracks are created, only one can be closed by
 210 external uniaxial loading.

$$D_I^{c,ISR} = 1 - \left((1 - D_{II}^{t,ISR})(1 - D_{III}^{t,ISR}) \right)^\alpha \quad (14)$$

211

212 α is a coefficient (nearly 0.15 in flexion tests [23]) that links compression and tension ASR damage
 213 (validated on experimental tests [24]). These two types of damage are included in the total stress
 214 formula (1).

215

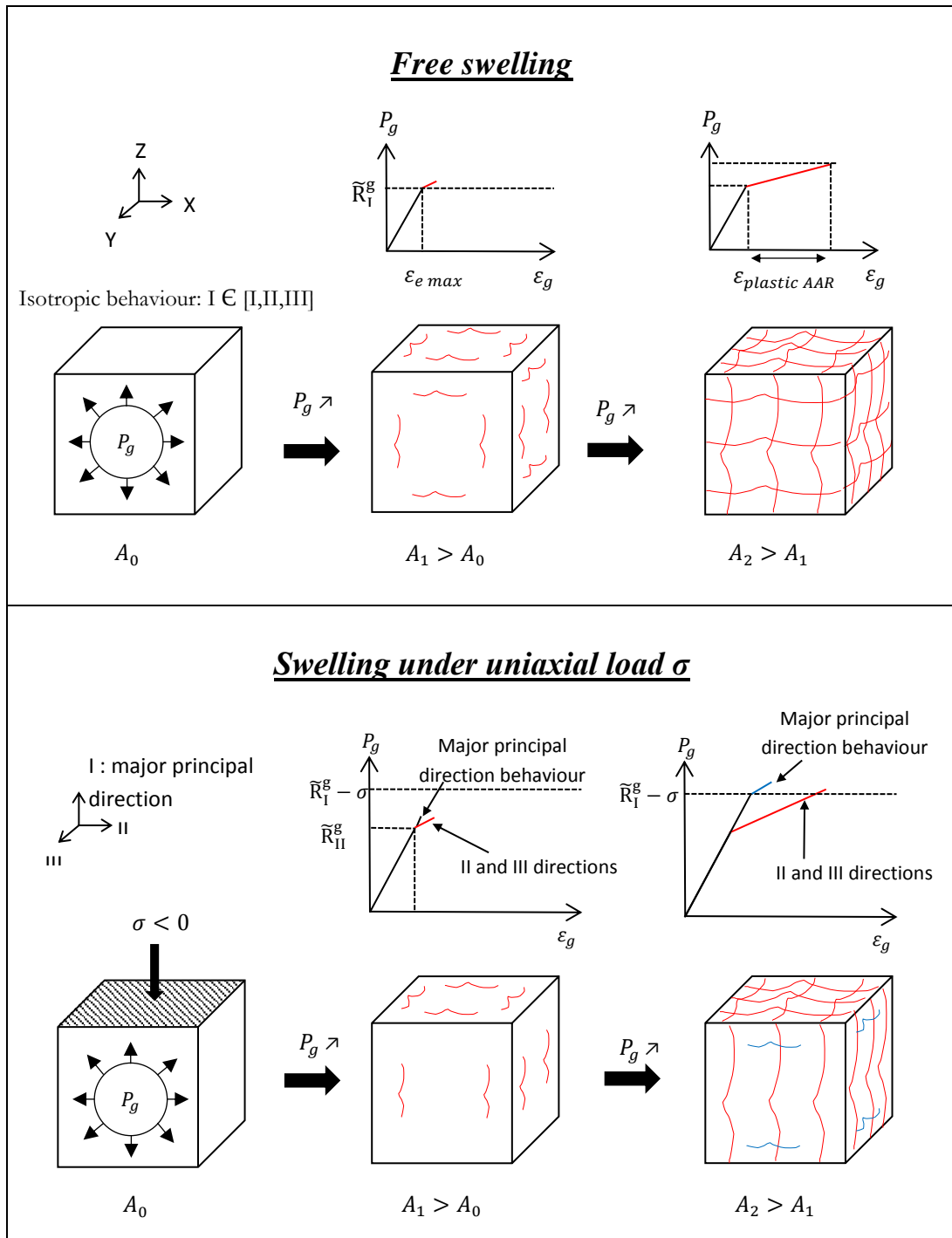
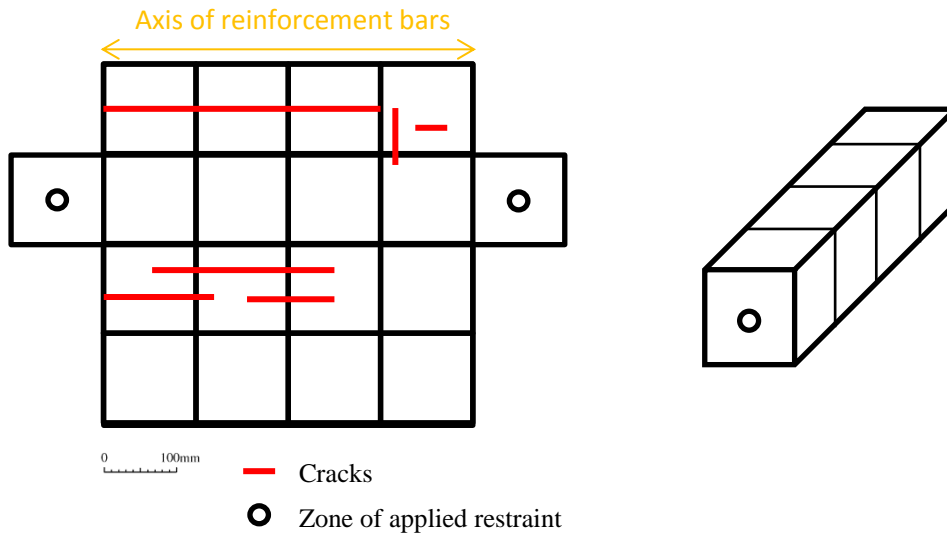


Fig. 3. Cracking kinetics in free swelling and in loading tests.



217

218

Fig. 4. Unfolded diagram of crack patterns in a concrete prism [21].

219

Table III summarizes the ASR model parameters.

<u>Parameter</u>	<u>Symbol</u>
Advancement	
ASR characteristic time	τ_{ref}^{asr}
Thermal activation energy	E^{asr}
Saturation degree threshold	$S_r^{th,asr}$
Poromechanics	
Maximum gel potential	ϕ_g^∞
Fraction of gel not effective in creating expansion	ϕ_g^v
Gel Biot coefficient	b_g
Gel Biot modulus	M_g
Cracking	
Plastic hardening ratio	h_{asr}

220

Table 3. ASR model parameters.

221

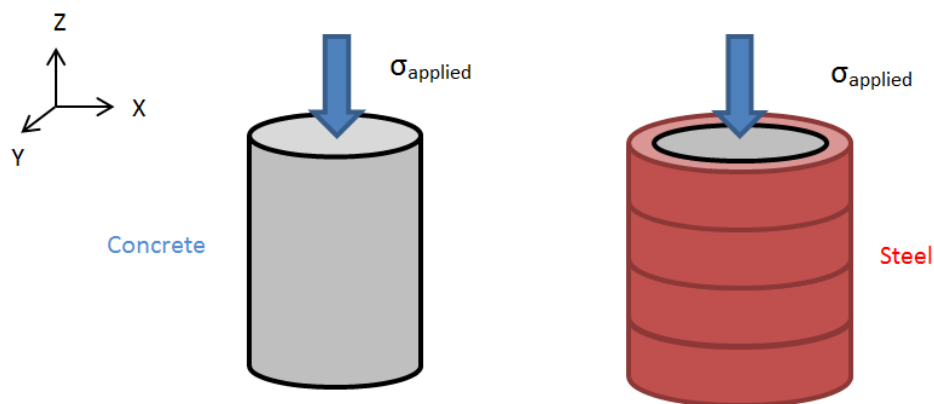
222 3. Validation and analysis of Multon's test

223 3.1. Experimental conditions

224 Numerical results were compared to the results of Multon's tests [10] in order to validate the
225 model. In this experiment, specimens were loaded in uniaxial compression and the radial displacement
226 was restrained by steel rings surrounding the concrete cylinders (Fig. 5). After fitting creep and
227 shrinkage on non-reactive material, the first step was the calibration of ASR parameters. A global
228 calibration was performed to validate the model with all restraints and loads.

229 During these experiments, a 28 days curing period was applied at 20°C. Then, the temperature
230 was increased to 38°C. Results are presented after the curing period. Shrinkage cylinders were sealed
231 with three layers of aluminium foil but they still showed a mass loss [10].

232 Before fitting material parameters, some physical values were measured: the tension strength
233 and Young's Modulus were equal to 3.7 MPa 37.2 GPa respectively.



234

235 Fig. 5. Scheme of Multon's tests.

236 3.2. Calibration methodology

237 Creep and shrinkage were first calibrated on a non-reactive specimen (Fig. 6). From the mass
238 loss, the environmental conditions and the fitting strains were reproduced faithfully through the Van
239 Genuchten law (two material parameters M_{sh} and b , Eq. 15 [25]). Then, creep tests at 10 and 20 MPa
240 simulated the material behaviour under long-term uniaxial loading. Four parameters were necessary to

241 fit the creep: two characteristic times for reversible and irreversible creeps, one for the modulus of the
242 reversible part and one characteristic strain for the irreversible part.

$$P_w = M_{sh} \left(1 - S_r \left(1 - \frac{1}{b} \right) \right)^{(1-b)} \quad (16)$$

243 During the first days of experimentation in the steel rings test, lateral concrete strains were
244 negative, meaning that the concrete and steel were no longer in contact. To avoid initial cracking or
245 use of an interface law, the Young's Modulus of the steel rings was numerically set close to zero until
246 strains became positive again.

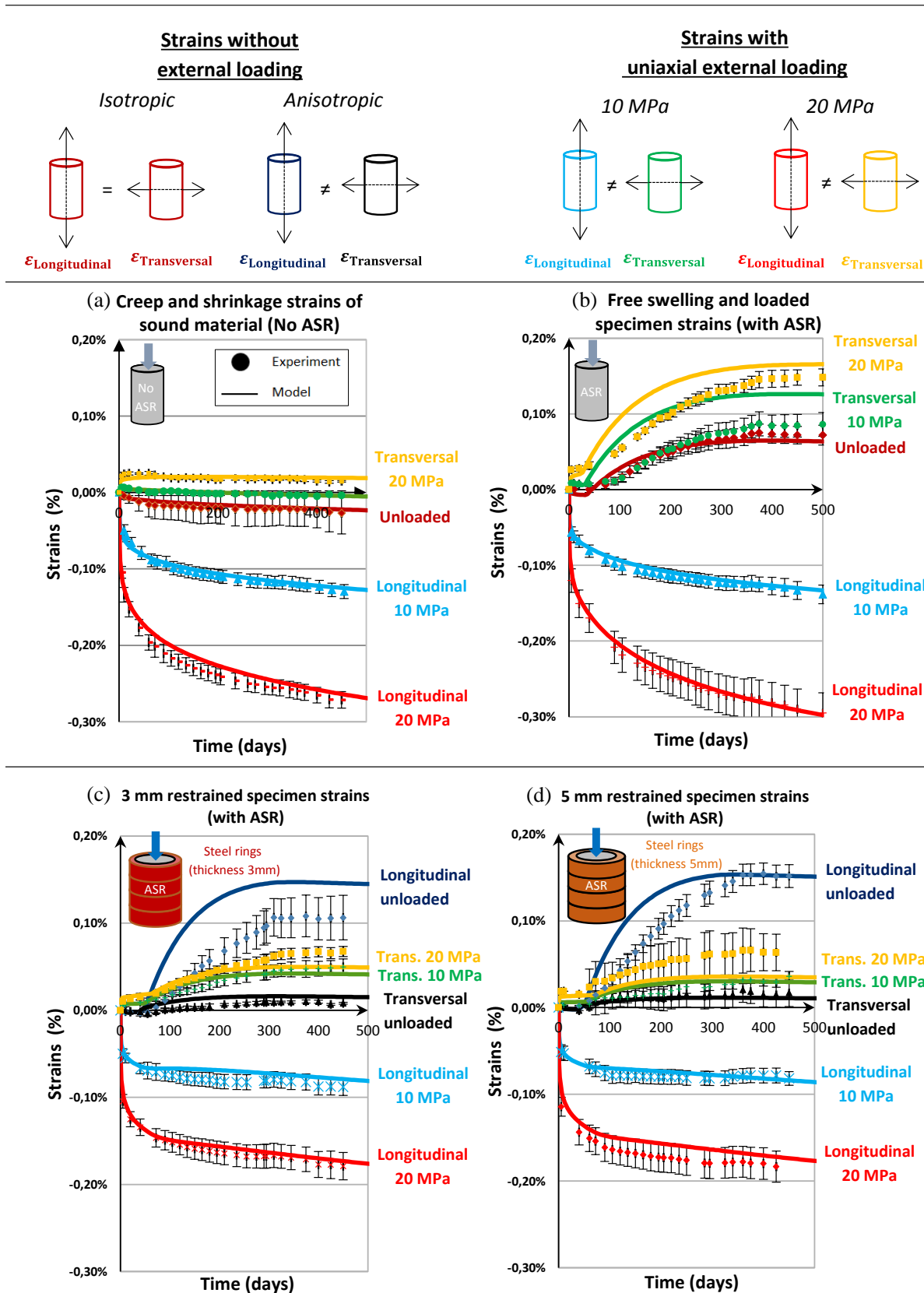
247 Then, the maximum gel volume, ϕ_g^∞ , and the fraction of non-effective gel, ϕ_g^∞ , were
248 calibrated by a free swelling test. Tests with steel rings put the material in multi-axial restraint. In this
249 state, the gel Biot coefficient, b_g , was fitted.

250 3.3. Calibration analysis

251 Fig. 6 shows that the model was able to reproduce ASR expansions under multi-axial loads and
252 restraints, and to approach most of the experimental results obtained in Multon's experiments.

253 For free swelling tests (without steel rings, marked (b) in Fig. 6), isotropic unloaded (brown)
254 and longitudinally loaded (blue and red) swelling curves were fitted; the behaviour was well
255 reproduced. Transversally (yellow and green curves), the kinetics given by the model was a little fast.
256 At the asymptote, the 20 MPa case was correctly reproduced but 10 MPa final strain was too high.
257 Experimentally, unloaded strain and transversal 10 MPa strain were quite similar while the loaded
258 strain was expected to be higher than the unloaded one (due to the Poisson effect).

259 For restrained tests ((c) and (d) in (Fig. 6), loaded tests were reproduced faithfully. Transversally,
260 stress free tests were well simulated (black curves). Longitudinally, the kinetics was a little fast. Final
261 strain was correct for the 5 mm test (dark blue curve on (d)) but too high for the 3 mm test (dark blue
262 curve on (c)). These experimental points seem to be very different in the 3 and 5 mm tests whereas
263 values are close for all other tests with steel rings.

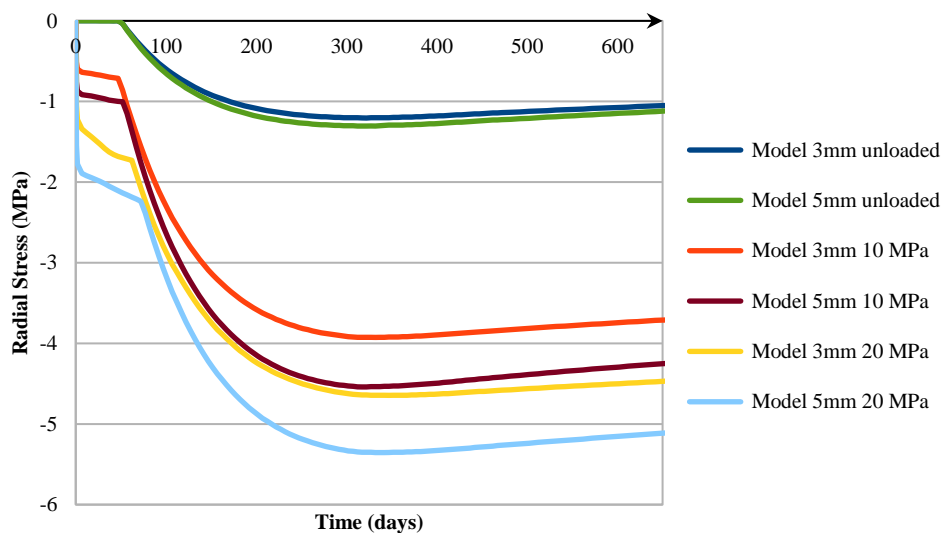


264
265
266
267

Fig. 6. Multon's test results for strains [10] : (a) creep and shrinkage without ASR, (b) ASR free swelling tests and loaded tests, (c) 3 mm restrained tests, (d) 5 mm restrained tests ($R_t=3.7$ MPa; $\phi_g^\infty=0.0054$ m³/m³; $\phi_g^v=0.0013$ m³/m³ $b_g=0.25$; $M_g=27700$ MPa; $h_{\text{ASR}}=0.03$)

268 Due to ASR expansion and the Poisson effect on loaded tests, radial stresses developed on
 269 these rings. These stresses were extracted from the calculations (Fig. 7). Model results gave radial
 270 stresses between 1.2 and 5.4 MPa (compression stresses). Radial stress curves contained four parts: the
 271 application of external stress (between 0 and 1 day), the latency period before expansion became
 272 significant (between 1 and 80 days), the expansion period (between 80 and 350 days) and the part
 273 where the reaction was over and shrinkage became the main deformation phenomenon.

274 During the latency period, radial stress was nearly zero for unloaded specimens because
 275 shrinkage was greater than the gel pressure, so the concrete and the steel rings were not in contact.
 276 Specimens with 3 mm thick steel rings showed smaller radial stress than specimens with 5 mm thick
 277 rings because of the difference of rigidity.

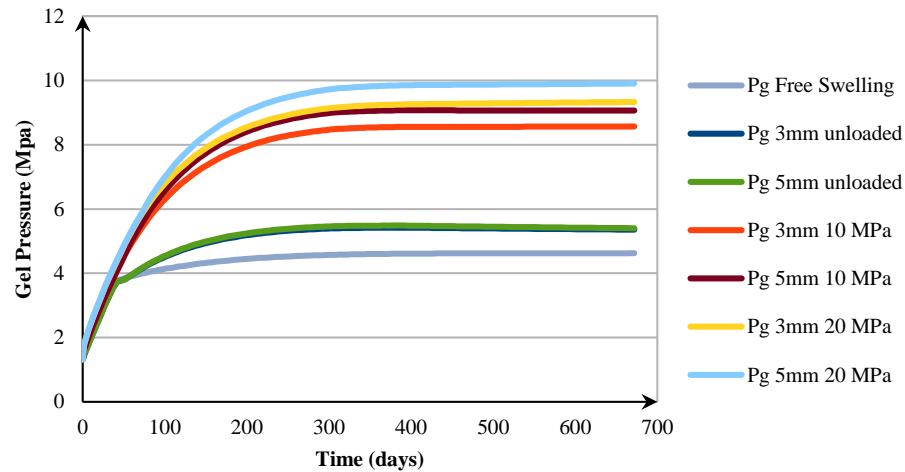


278

279 Fig. 7. Radial stresses obtained from the model.

280 The start of expansion depended on the applied stress. The evolution of P_g was proportional to
 281 the strains. The increase of the stress in 5 mm thick steel rings was more significant because the
 282 rigidity slowed the radial strain (for the same applied stress). The more restrained the cylinder was, the
 283 faster the radial stress increased (Fig. 7). At 650 days, the gel pressure, representing the average
 284 pressure transferred to the aggregate surface, varied from 4.6 MPa to 10.0 MPa according to the stress
 285 state (Fig. 8). As expected from the model equations, the maximum pressure was obtained for the

286 concrete with the greatest loading (20 MPa) and restraint (5 mm). From 350 days to the end of these
287 experiments, stresses decreased. Shrinkage became the main phenomenon in this period.



288

289

Fig. 8. Gel pressure from the model in tests.

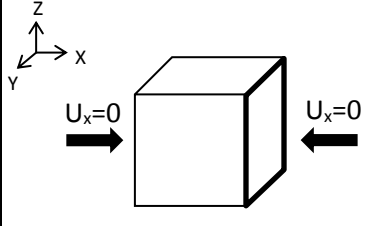
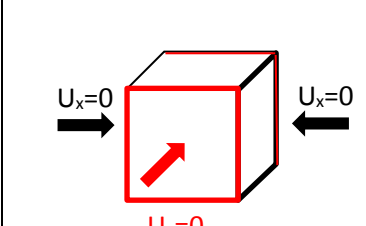
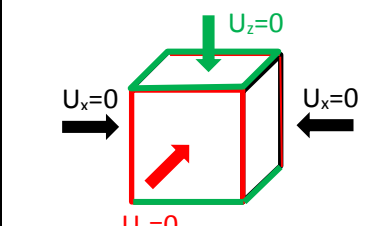
290 4. Impact of restraint

291 Based on calibration using Multon's tests, the model reproduced the effects of stresses and
292 restraints on ASR expansion faithfully. In these tests, the rigidity of the steel rings was not infinite.
293 They were deformable whereas, in reality, restraint can be more rigid (in the case of a dam for
294 example).

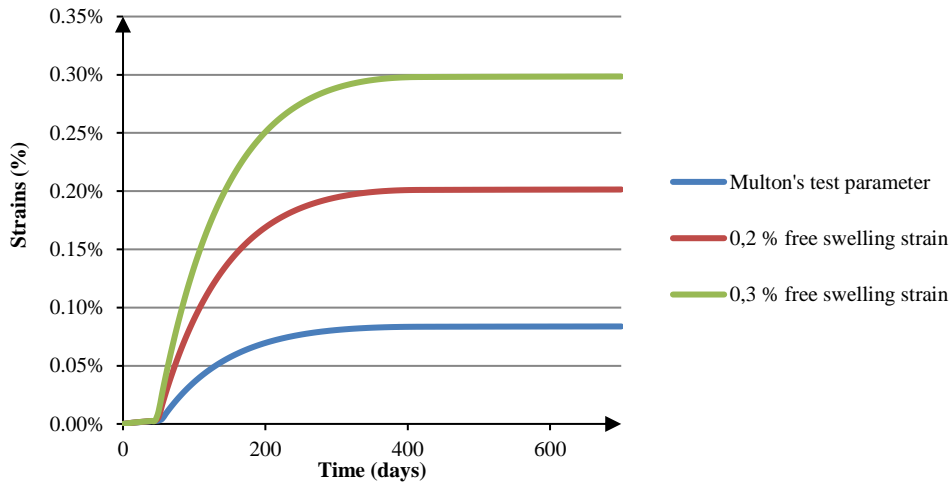
295 This part describes a theoretical test performed in order to analyse the effects of perfect
296 restraint on ASR-expansion (displacement equal to zero in blocked directions). The aim was to
297 compare the behaviours of expansive concrete with restraints or applied stress (in the next part). To
298 facilitate the modelling of mechanical boundary conditions, a cube was modelled. It was restrained in
299 from one to three directions (Table 4). In order to analyse the concrete behaviour under ASR-pressure
300 only, the tests were calculated without shrinkage. This avoided problems of debonding between the
301 boundary condition and the concrete. Stresses were applied after 28 days.

302 In Multon's free swelling test, the strain at 700 days approached 0.08 % (without shrinkage).
303 For these theoretical tests, ASR maximum volume was fixed in order to obtain a usual but larger
304 expansion - equal to 0.3%. Fig. 9 shows the calculations for a strain of 0.3% with a maximum gel

305 volume $\phi_g^\infty = 0.03 \text{ m}^3/\text{m}^3$ and a fraction of non-effective gel $\phi_g^\infty = 0.008 \text{ m}^3/\text{m}^3$. Numerical tests
 306 in restrained conditions were performed with these parameters.

Swelling restrained in one direction	Swelling restrained in two directions	Swelling restrained in three directions
		

307 Table 4. Boundary conditions of theoretical tests.



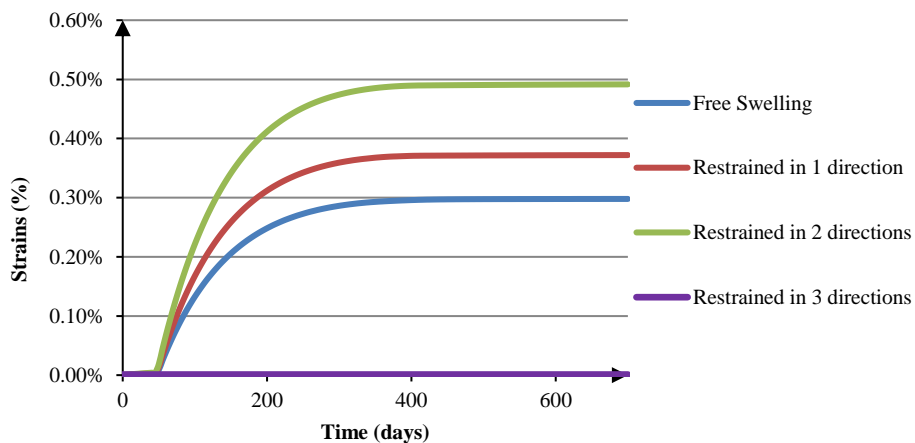
308
 309 Fig. 9. Comparison of free swelling strains.

310 First, strains in free directions were compared (Fig.10). Strain in free directions increased by
 311 25% compared to stress free expansion when the cube was restrained in one direction and by 65%
 312 when it was restrained in two directions.

313 After running a free swelling test and multi-direction perfectly restrained expansion tests,
 314 stresses were extracted (Fig. 11). The stress in restrained conditions could be described in two phases:
 315 a slow increase of the stress before first cracking (0 to 80 days), then fast increase after first ASR
 316 damage. For these conditions of perfect restraint, the maximum stress lay between 3 and 7 MPa of
 317 compression (for 1 to 3 restrained directions). It should be noted that final stress was not directly
 318 proportional to the number of restrained directions. Gel pressure rose strongly if three directions were
 319 restrained because this constituted full confinement. If the free maximal strain was 0.3%, an isotropic

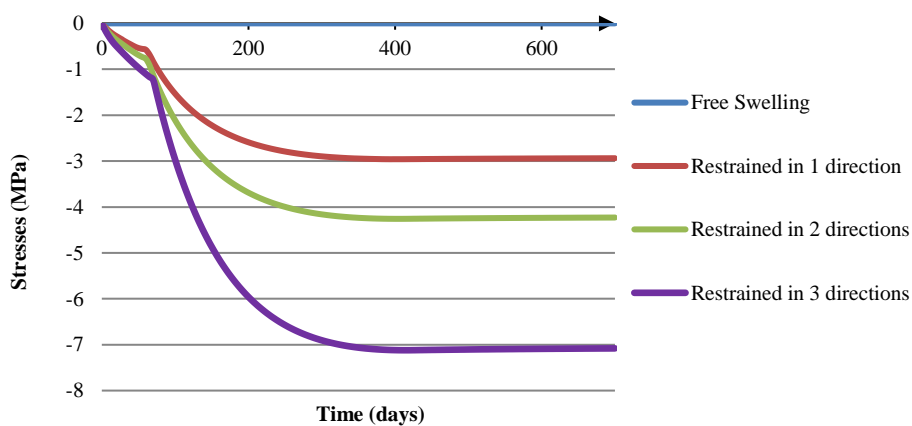
320 thermo-elastic calculation gave a stress of 113.1 MPa ($E_c \cdot \epsilon = 37700 * 0.003$). Taking usual standard
 321 creep into account with an effective Young's modulus ($E_c = E_{c0}/3$), the result was still 37.7 MPa. These
 322 results are not consistent with experimental results [10]. Finally, it is very interesting to note the good
 323 agreement between the compressive stress of 3 MPa obtained for 1 D restraint and stresses usually
 324 observed in dams restrained in one direction [26]. This is also a good justification for using this type
 325 of modelling to represent anisotropy of expansion with stresses in real structures.

326 For specimens with 2 or 3 restrained directions, the maximum compressive stress increased,
 327 reaching 4 and 7 MPa respectively. This result depended on the capacity of ASR-gels to move in the
 328 concrete porosity. Under such pressures, ASR-gels could permeate further through aggregate and
 329 concrete porosity than in the stress free conditions taken into account in the pressure equation (8).



330

331 Fig.10. Comparison of strains in free swelling and restrained tests.



332

333

Fig. 11. Comparison of stresses in free swelling and restrained tests.

334 In the next part, stresses obtained in these tests are applied instead of restraints to analyse the
335 differences between the effect of restraint and the effect of stress on ASR-expansion. For example, for
336 the 3-direction restrained tests, stresses are applied from 0 to 7 MPa in these directions.

337 **5. Impact of stresses**

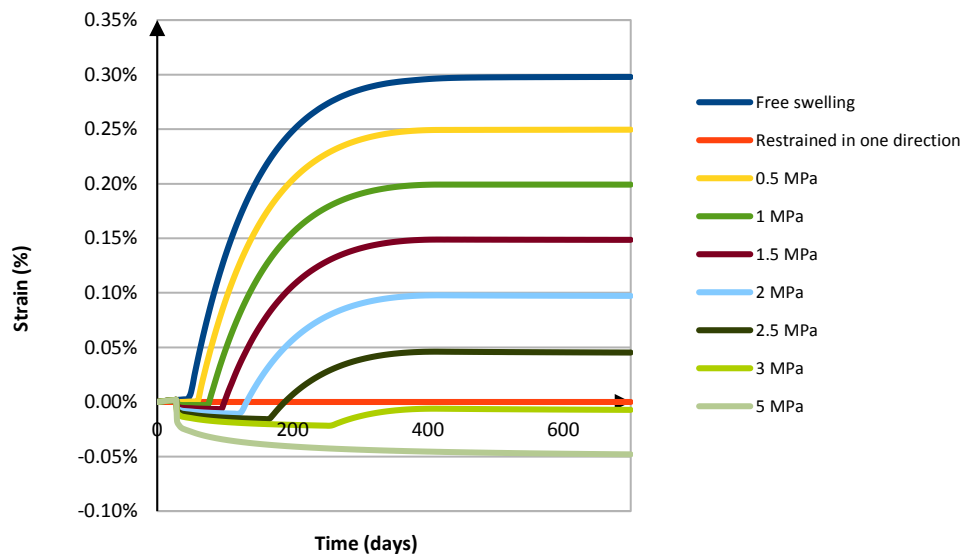
338 *5.1. Compressive stress*

339 Many structures (prestressed ones for example) are subjected to compressive stresses before
340 ASR swelling appears. The aim of this part is to compare the behaviours of restrained structures and
341 structures subjected to stress during ASR swelling.

342 For the specimen restrained in one direction, induced stresses were between 0 and 3 MPa.
343 Here, they were applied in increments of 0.5 MPa. Fig. 12 shows the strains obtained for different
344 loads in the stress direction. The larger the applied stress, the smaller the final strain. Above 1 MPa of
345 compressive stress, the latency period depended on the stress state because creep strains were larger
346 than the strains induced by the gel pressure. This period varied from 50 to 245 days. For the 3 MPa
347 test (close to the maximum pressure obtained in the restrained test), the final strain was close to 0.
348 Strain decreased proportionally to applied stress. The modelling was thus consistent when expansions
349 under restraint and under applied stress were compared. According to the stress amplitude and ASR-
350 latency time, creep was first predominant in the concrete behaviour. The final difference between
351 restrained and applied stress tests was due to creep. The 5 MPa case (Fig. 12) showed that there was
352 no swelling after a compressive stress threshold (here between 3 and 5 MPa). There was no cracking
353 in the loading direction. In Larive's tests [14], a 5 MPa uniaxial compressive stress was applied to the
354 specimen. Cracks only appeared parallel to the loading direction, while cracking was isotropic in the
355 stress free specimen.

356 Fig. 13 shows the damage in the loaded and free directions for the 3 MPa loading test (one
357 direction loaded). The first damage was in the unloaded direction and then the loaded direction was
358 slightly damaged (here for a coefficient $h_{\text{ASR}} = 0.03$). There was a delay between the start of cracking
359 in the different directions, as explained in Fig. 3. The free direction was less damaged than the loaded

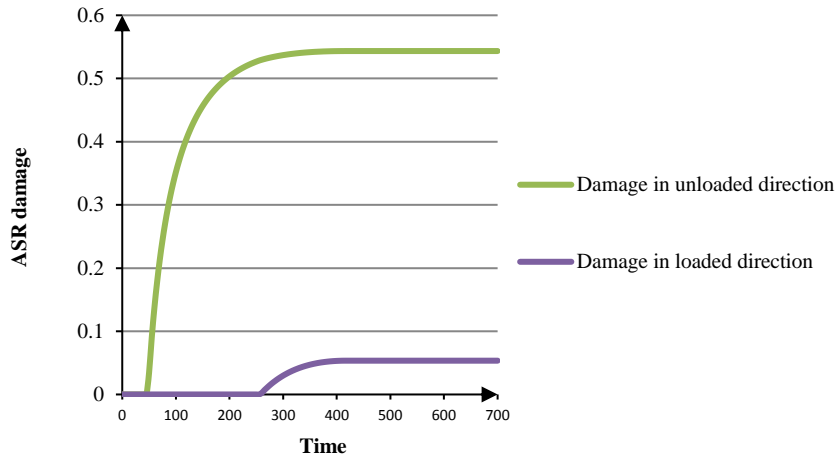
360 direction. This represents the effect of compressive stress on the anisotropy of cracking due to ASR-
 361 expansion. The difference depends directly on the applied stress. For a smaller stress, the damage
 362 perpendicular to the loaded direction is greater while, for a stress higher than about 3 MPa, we can
 363 expect to obtain no damage perpendicular to the loaded direction. As damage directly affects the
 364 Young's modulus, the material becomes anisotropic; the Young's modulus will be smaller in the free
 365 direction while the mechanical performances are less affected in the loaded ones.



366
 367 Fig. 12. Strains in loaded or restrained direction.

368 ASR damage is not linearly proportional to the stress applied (Fig. 14) and, in the model, the
 369 material parameter $\varepsilon^{k,ISR}$ (ASR characteristic strain) allows this phenomenon. It weights ASR plastic
 370 strains when calculating ASR damage (13). Furthermore, when the stress was applied, gel pressure
 371 had to reach a higher value in order to exceed the cracking criteria. This took time and damage became
 372 delayed. When the specimen was restrained in one direction, it became damaged more rapidly as soon
 373 as the swelling began but the damage development was slowed down because the induced
 374 compressive stress also increased slowly. Finally, restraint test specimens can be compared to
 375 reinforced structures and applied stress test specimens to concrete structures such as bridge piers or
 376 prestressed beams.

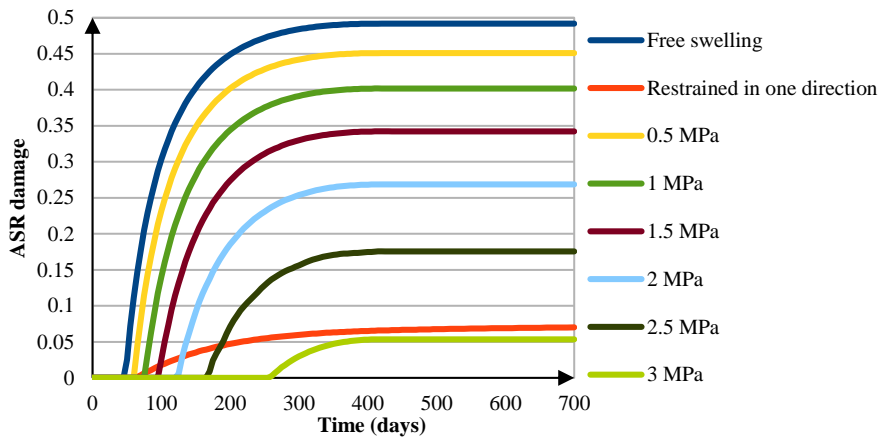
377 Numerical results on the effect of stress can be compared to those obtained with Charwood's law [3]
 378 (17).



380

381

Fig. 13. ASR damage in the 3 MPa test (applied in one direction).



382

383

Fig. 14. Damage in loading direction (one direction loaded or restrained).

$$\varepsilon = \begin{cases} \varepsilon_u & \text{if } \sigma \leq \sigma_l \\ \varepsilon_u - K \log_{10} \left(\frac{\sigma}{\sigma_l} \right) & \text{if } \sigma > \sigma_l \end{cases} \quad (17)$$

384

When the applied stress σ is smaller than the stress threshold σ_l , the strain is equal to ε_u (a material

385

parameter). When the applied stress σ exceeds the threshold σ_l , the strain decreases from ε_u to zero.

386

K is a material parameter that fits the slope of the decrease.

387

In Fig. 15, the parameter K from Charlwood's law has been fitted with the least squares

388

method on 1D model results ($K = 0.0027$, $\varepsilon_u = 0.003$, $\sigma_l = 0.3 \text{ MPa}$). Charlwood's law is more non-

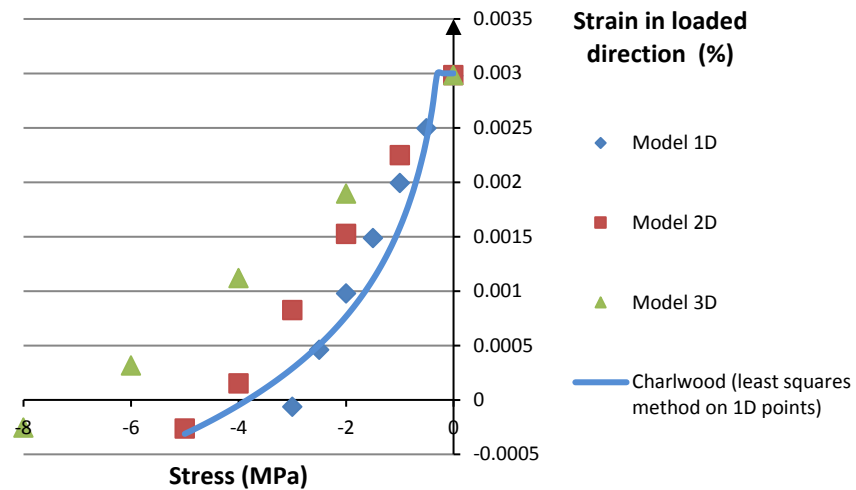
389

linear than this model (Fig. 15) and it does not consider differences of behaviour between uniaxial and

390

multi-axial loading. For this fitting, Charlwood's law strain is close to the model in 1D for small

391 stresses (< 3 MPa). In the 2D case, the stress needed to obtain a strain equal to zero is nearly the same
 392 in both models (≈ 4 MPa). However, Charlwood's law gives more non-linear results for lower stresses.
 393 The model proposed here considers the confinement effect in the gel pressure equation (Eq. 18). This
 394 explains some differences between 1D, 2D and 3D.



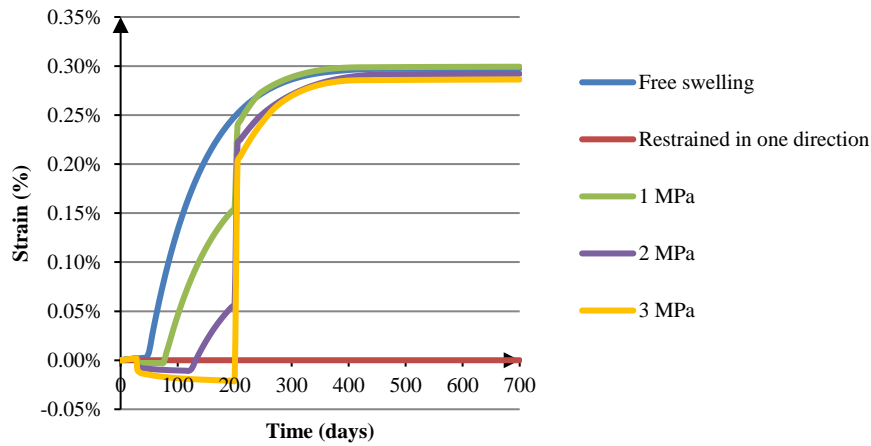
395
 396 Fig. 15. Strains obtained from the model in multi-axial loadings
 397 and from Charlwood's law [3].

398 5.2. Impact of unloading

399 In this part, the impact of unloading during swelling is studied. When an owner tries to
 400 understand the ASR damage in his damaged structure, core drilling is often used. This action leads to a
 401 relaxation of stresses in the sample taken. It can also represent the breaking of a prestressed bar. The
 402 material used here was the same as in part A. Specimens were loaded at 28 days and unloaded at 200
 403 days (for an ASR-advancement of about 0.7).

404 In the loaded direction, strains were negative after application of the load, because of concrete
 405 creep, and before ASR swelling, according to the applied stress value (Fig. 16). When the material was
 406 unloaded, the strain in this direction occurred very fast and tended towards the free swelling strain
 407 value. This result confirms the analysis performed in [27]. The final difference between free swelling
 408 and unloaded tests strains was small but proportional to the applied stress. It was due to the
 409 irreversible creep strain reached before swelling. When the stress was removed, strain in the initially
 410 unloaded direction stopped growing and all the swelling went to the initially loaded direction (Fig.

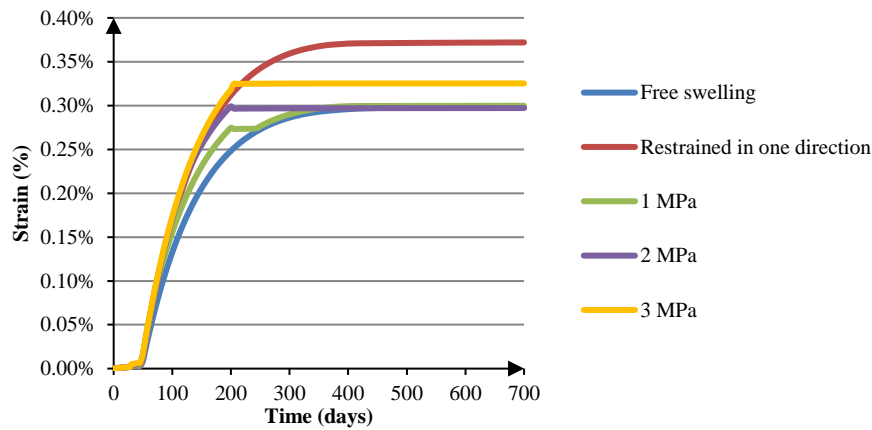
411 17). At this time, the ASR criterion in the initially loaded direction was reached instantly: it passed
 412 from $\bar{R}_I^g - \sigma$ to \bar{R}_I^g , the tensile strength of the concrete (Fig. 3). There was a jump in displacement.



413

414

Fig. 16. Strains in initially loaded direction.



415

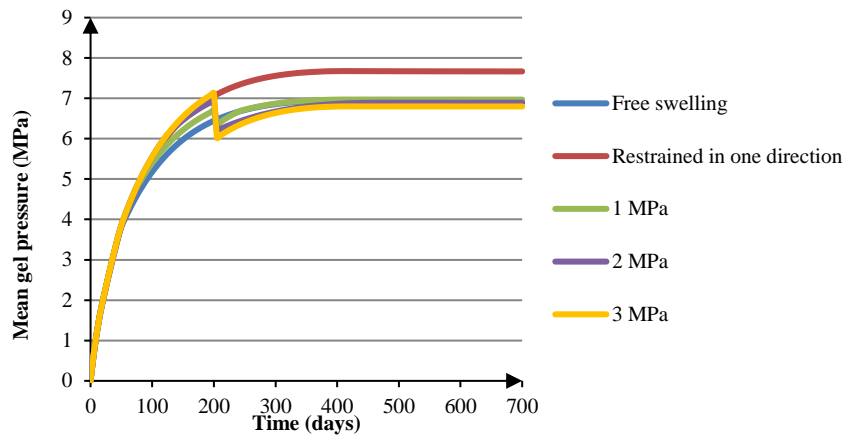
416

Fig. 17. Strains in initially unloaded direction.

417 In the initially unloaded direction (Fig. 17), at 200 days, strains decreased slightly. When
 418 strong swelling is in progress on an initially loaded direction, ASR plastic strains $\varepsilon^{p,g}$ increase fast. In
 419 (8, this strain directly impacts the mean gel pressure, which decreases abruptly (Fig. 18). Therefore,
 420 the ASR strain lost part of its elastic strain. This explains the decreased strains in the initially unloaded
 421 direction. In reality, this effect can be decreased by ASR-gel exudations as noted by [28]. When gels
 422 permeate out of drilled cores, pressure decreases brutally and expansion can slow down and stop. In
 423 any case, this modifies the expansive behaviour of the concrete.

424 Due to stress release and its impact on expansion, unloading could imply high ASR damage in
 425 the initially loaded direction (Fig. 19) whereas there was no damage in this direction when the

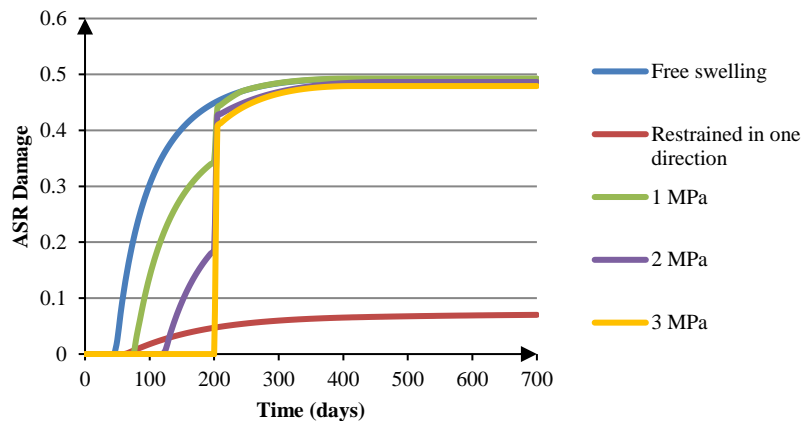
426 concrete was under loading in the structure. In consequence, new damage could be encouraged by
 427 unloading or drilling. Mechanical or residual expansive tests, performed with such drilled cores, could
 428 be negatively impacted by this damage, which is not really present in the structure. Using such a test
 429 for predictive calculations could then be hazardous.



430

431

Fig. 18. Gel pressure variation in unloading tests.



432

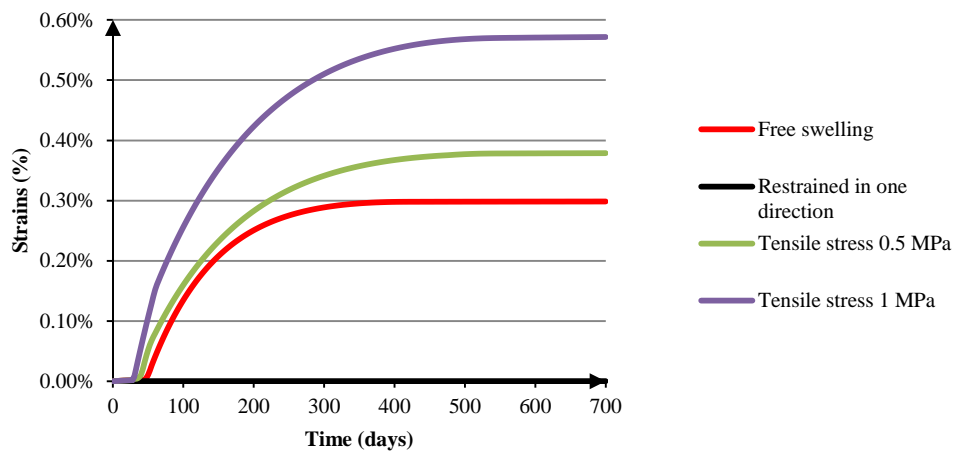
433

Fig. 19. ASR damage in initially loaded direction.

434 5.3. Tensile stress

435 In order to complete the theoretical analysis, the same kinds of tests were performed with
 436 tensile stress. Here, specimens were loaded in one direction only with tensile stresses of 0.5 and 1 MPa
 437 (a higher value cannot converge due to coupling of the tensile damage with ASR damage, which leads
 438 to specimens cracking). Strains in the loaded direction are summarized and compared to free swelling
 439 in Fig. 20. First, it is important to note that tensile stress accelerated the ASR swelling (Fig. 21). This
 440 can be explained by the ASR plastic criterion being reached sooner for tensile stress. Secondly, the

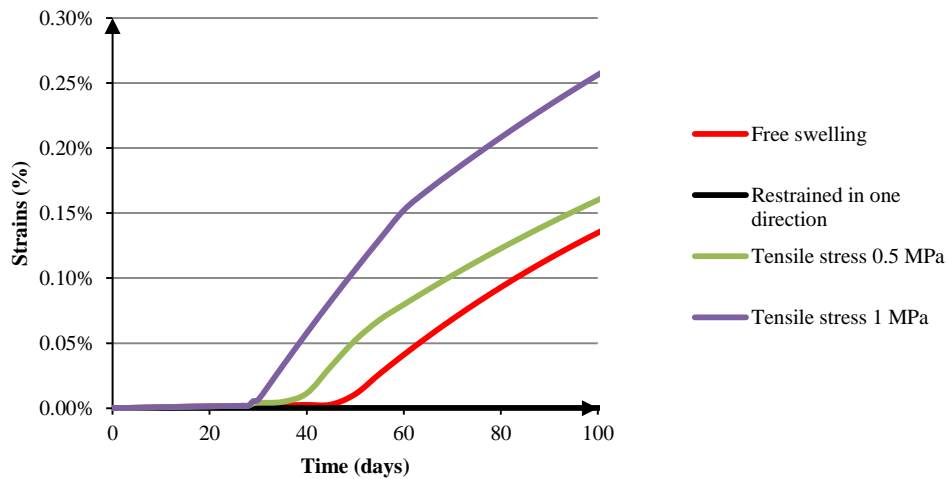
441 final strain induced by expansion in concrete subjected to tensile stresses increased (Fig. 20). In real
 442 structures, tensile stresses can be induced by moisture gradients and restrained. Thus, in reinforced
 443 concrete, the tensile cracking criterion could be reached first, due to restrained shrinkage before ASR
 444 expansion. This could finally accelerate the apparition of the first expansion compared to stress free
 445 conditions. However, once swelling occurs, compressive stresses will rise due to expansion restraint
 446 and expansion will decrease compared to expansion without compressive stress.



447

448

Fig. 20. Strains in restrained or loaded direction.



449

450

Fig. 21. Strains in restrained or loaded direction (zoom on 0-100 days).

451

452

453

Consecutively, ASR damage increased with the load in loaded directions (Fig. 22) as the solid skeleton had to support concurrent stresses: gel pressure and structural stress. Damage was non-linear because of the ASR characteristic strain $\epsilon^{k,isr}$ (13).

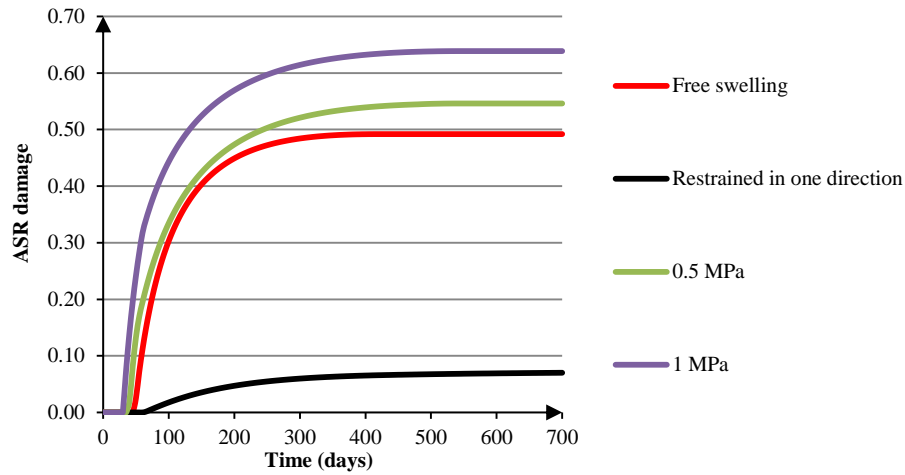
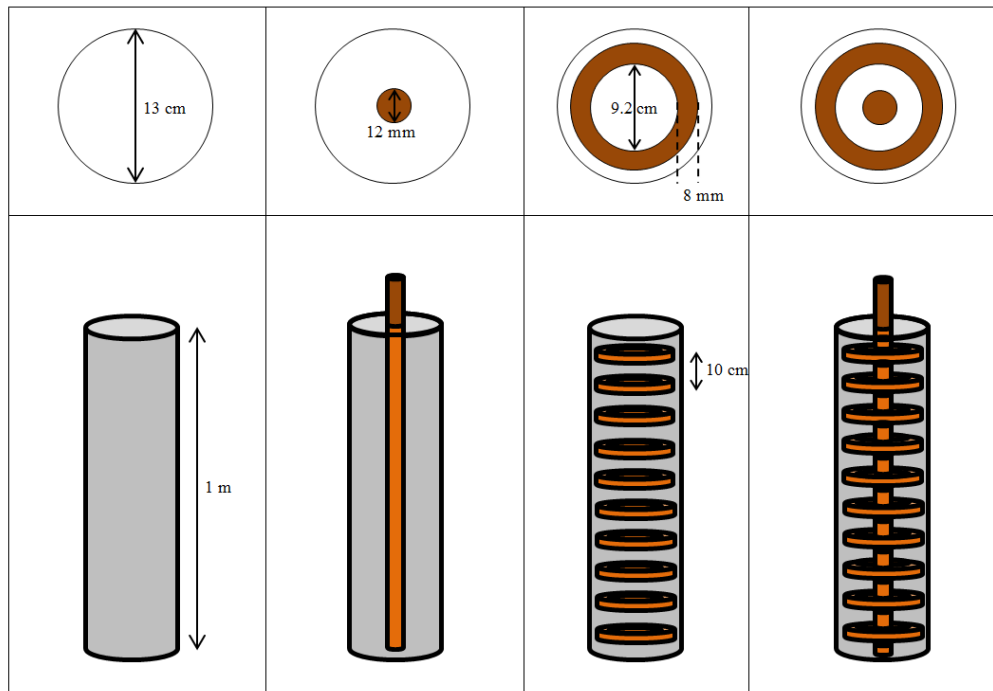


Fig. 22. ASR damage in restrained or loaded direction.

6. Impact of reinforcement on ASR-expansion

In many damaged structures, the effect of stresses on ASR expansion is mainly due to restraint by reinforcement. In this part, the impact of reinforcement on specimens subjected to ASR is analysed on the basis of the calibration obtained for Multon's tests, which quantified the impact of stresses on ASR-expansion. The focus is particularly on the anisotropic effect of reinforcement and on induced stresses.

In order to approach the behaviour of structures, real conditions were simulated: the shrinkage was taken into account and steel was used instead of perfect restraints. The main specimen was a concrete cylinder 1 metre high and 13 centimetres in diameter (Table 5). First, free swelling gave a reference of isotropic values for damage and strain. Then, anisotropy was induced by longitudinal ribbed bars and steel rings, which could represent the effect of stirrups on expansion. One test consisted of adding a longitudinal ribbed steel bar (diameter 12 mm, i.e. 0.85% of steel section) in the centre of the specimen. Another one consisted of adding steel rings (8x8 mm section) every 10 centimetres. The last test was performed with both the longitudinal ribbed bar and the steel rings (Table 5).



471

472

Table 5. Scheme of specimen geometries.

473

474

475

476

477

478

479

480

481

482

483

In terms of anisotropy, the ratio of the longitudinal and transversal strains (respectively ε_L and ε_T) to the longitudinal and transversal strains in the free expansion condition (ε_{WR}) were compared for each test (Table 6). The longitudinal ribbed bar had a strong impact on longitudinal strain: about 50% of its initial value. The transversal strain increased by 20%. In the case of steel rings, longitudinal strain increased (30%) while transversal strain decreased (to 50% between the longitudinal axis and the rings). When both reinforcements were used, longitudinal strains were reduced to half (between 40 and 60% of the free swelling value). Transversally, the difference depended on the location: between the ribbed bar and a ring, concrete was confined and strains were reduced by 35%. However, between two rings, strains grew due to the reinforcement in the transversal direction, as restrained parts helped to increase the strain in this direction. These results are drawn on the deformed shapes of specimens in Table 7.

484

485

486

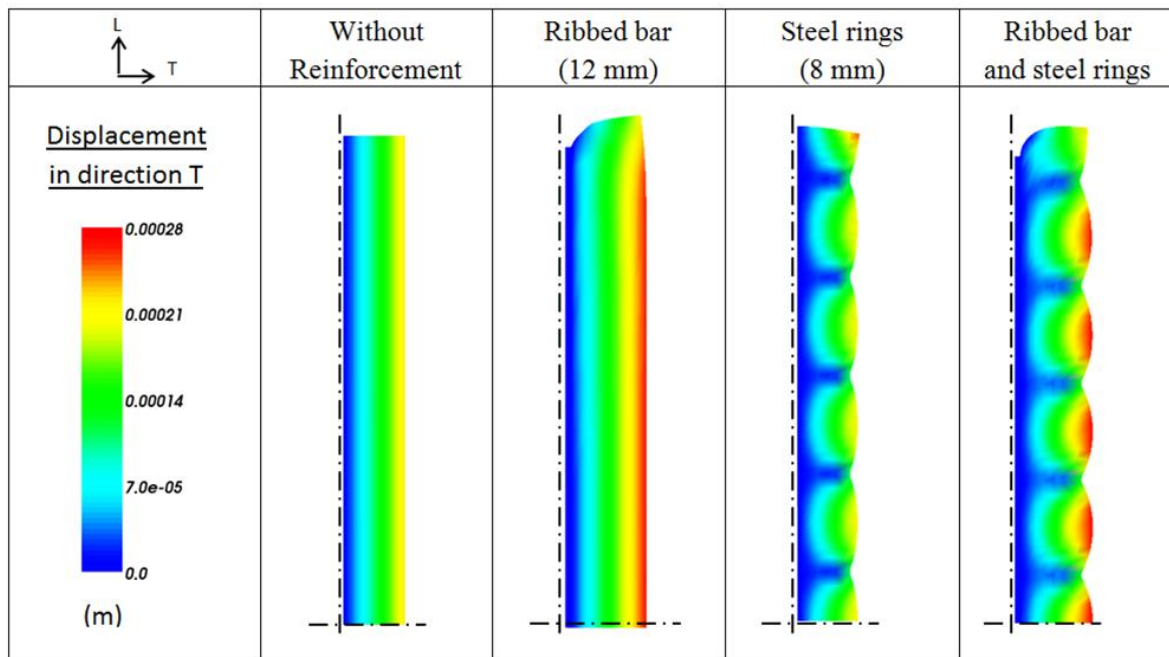
487

Table 6 also gives stress values inside the concrete and the steel. In concrete, the confinement increased the compression stress value (from 0 to 3.3 MPa). In the steel bar, stress could reach 300 MPa when the confinement was strong. Here, it is not sufficient to induce lamination of the steel but it is primordial if the steel is designed as a structural part.

	Without Reinforcement (WR)	Ribbed bars (12 mm)	Steel rings (8 mm)	Ribbed bars and steel rings
$\frac{\varepsilon_L}{\varepsilon_{WR}}$	1	From 0.3 (<i>close to the top</i>) to 0.5 (<i>close to the axis of symmetry</i>)	1.3	From 0.4 (<i>close to the top</i>) to 0.6 (<i>close to the axis of symmetry</i>)
$\frac{\varepsilon_T}{\varepsilon_{WR}}$	1	1.2	From 0.5 (<i>inside a ring</i>) to 1.0 (<i>between rings</i>)	From 0.65 (<i>inside a ring</i>) to 1.25 (<i>between rings</i>)
$\sigma_{MIN\ concrete}$ (MPa)	0	-1.8 (<i>parallel to the longitudinal axis</i>)	-0.7 (<i>perpendicular to the longitudinal axis</i>)	-3.3 (<i>between the bar and a ring</i>)
$\sigma_{MAX\ steel}$ (MPa)	-	195	110	300

488

Table 6. Test results.



489

490

Table 7. Displacement in transversal direction T, drawn on the deformed shape.

491

Table 8 shows the distribution of longitudinal and transversal ASR plastic strains (respectively

492

ε_{LASR}^{pl} and ε_{TASR}^{pl}) on a quarter of the geometry (symmetrical conditions). ASR damage, and thus the

493

impact of ASR on the mechanical properties of the concrete, can be calculated from these plastic

494

strains with (13): a plastic strain of 0.3% corresponds to ASR damage of 0.5. In the longitudinal ribbed

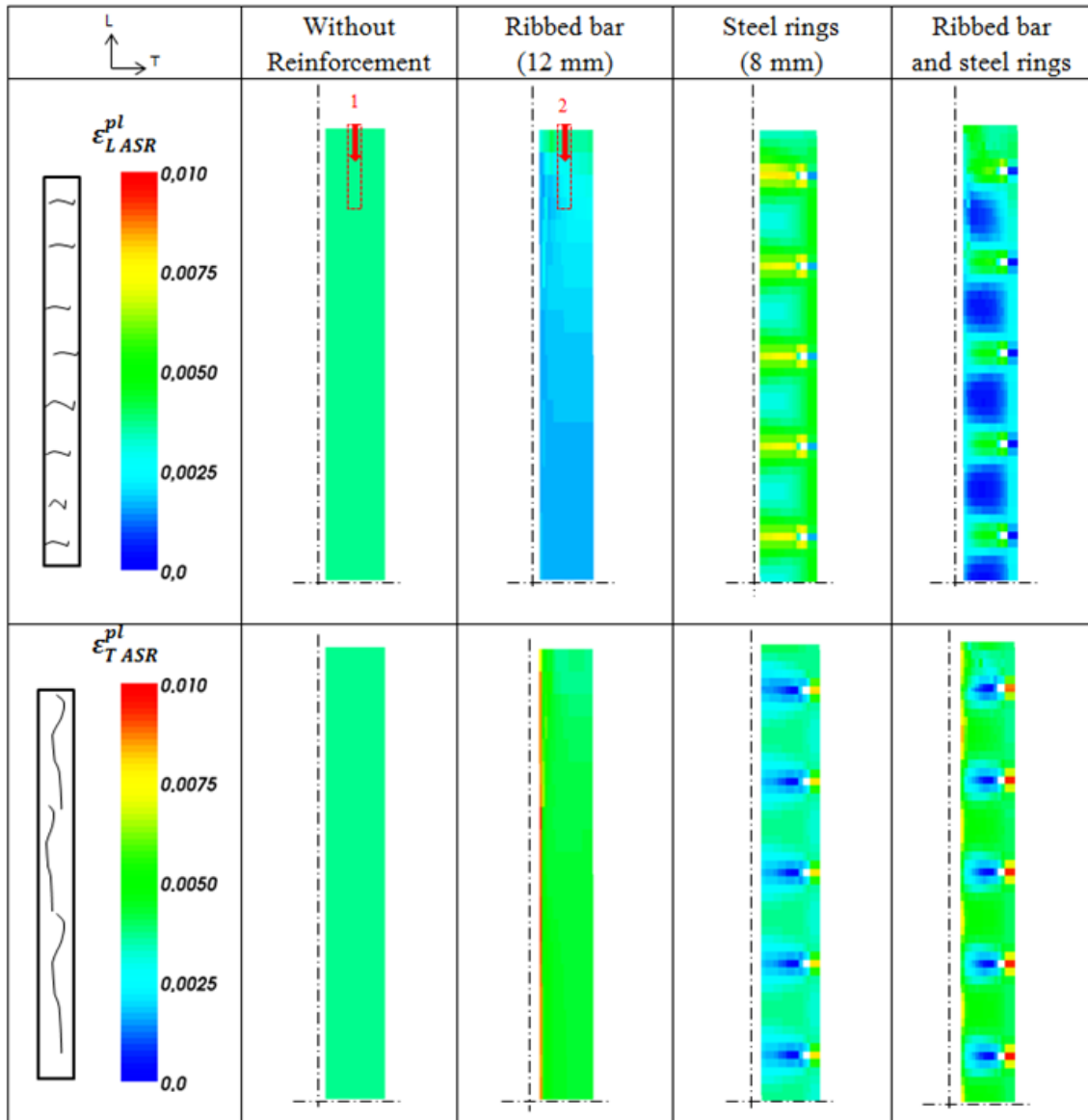
495

bar test, transversal ASR strains ε_{TASR}^{pl} were high in the steel-concrete contact zone because the steel

496 bar restrained the swelling concrete in the other direction. This zone acted like a joint and expansion
497 caused a debonding effect. This result is consistent with experimental results, which exhibit a decrease
498 of ultimate bonding strength in the case of specimens without stirrups [29–31]. For the steel rings test,
499 the maximum ASR plastic strain occurred near the rings in the longitudinal direction. The swelling
500 was restrained in the transversal direction and strains were thus mainly longitudinal in that place
501 because of anisotropy. This implies considerable damage in the longitudinal direction (transversal
502 cracks). In the transversal direction, the maximum plastic strain was far from the steel rings as the
503 swelling of the external concrete was restrained by the rigidity of the rings. When the ribbed bar and
504 steel rings were used together, the debonding effect was still noticeable but just between rings. The
505 rings restrained material expansion in the core of the specimen, which prevented debonding of the
506 longitudinal bar. There was less damage inside the steel rings due to confinement by the bar. However,
507 there was more damage outside because the concrete strains between the rings were greater than in the
508 previous test. According to the importance of restraint (number of stirrups compared to the concrete
509 section), the ultimate bonding strength could increase as observed qualitatively in [29]. Otherwise,
510 cracking could be delayed under external loads thanks to ASR prestressing in reinforced structures.
511 Experimentally, a reinforced wall was affected by ASR cracks later than a sound one [32].

512 It is interesting to analyse the effect of reinforcement on cracking anisotropy and the impact on
513 the analysis of structures for future prognosis. Table 8 shows two core samples drilled in the same
514 place in specimens in stress free conditions (marked as 1 in Table 8) and with a longitudinal ribbed bar
515 (marked 2). The first sample, taken in the free swelling test exhibits ASR isotropic damage of about
516 0.5 (corresponding to a plastic strain of 0.3%). The second one, extracted from the longitudinal ribbed
517 bar test, exhibits ASR cracks mainly oriented parallel to the bar (ASR damage: 0.65). Due to restraint,
518 ASR damage in the other direction is about 0.35. Thus, if these cores were used to measure the
519 residual mechanical strength of concrete, the core drilled in stress free conditions would lead to a
520 decrease of 50% while the core drilled perpendicular to the reinforcement would lead to a decrease of
521 65% and the core drilled parallel to the reinforcement to a decrease of only 35%. Usually, affected
522 concrete properties are assessed from compression tests; therefore compressive damage is smaller

523 than tensile damage (14). For instance, the last tensile damage (65% and 35%) corresponded
 524 respectively to compressive damage of 27% and 12%. This difference is obviously important for
 525 future calculations since underestimating the Young's modulus can lead to a large overestimate of
 526 the structure deflection.



527

528

Table 8. Final ASR plastic strains obtained from tests.

529

530

531

532

The behaviour of reinforced samples and the impacts of compressive and tensile stresses on ASR-expansion have been explained. The flexural behaviour of ASR-damaged beams can be deduced of the previous analysis. In reinforced structures, the steel bars imply expansion restraint and thus chemical prestress. From Table 6, it can reach about 1.8 MPa to 3.3 MPa depending on stirrups

533 distribution. These stresses due to restrained expansion leads to an increase of the tensile strength and
534 to a decrease of the compressive strength in the reinforced structures. When the loading is applied, the
535 stress necessary to cause the cracking of the concrete is the tensile concrete strength plus the chemical
536 prestress. Compared to a non-reactive reinforced beam, mechanical cracking due to flexion is delayed
537 since the loading necessary to cause the cracking of the part of the structure in tension is higher. This
538 behaviour is confirmed experimentally [33] . In the parts in compression, the compressive strength is
539 decreased (about 1.8 MPa to 3.3 MPa). Indeed, structural cracking in uniaxial compressive test
540 without ASR is due to dilatancy in unloaded directions, it is called a shear damage. ASR expansion is
541 restrained by the reinforcement, strains are transferred in the other directions (Fig. 13). So, the
542 compressive strength is reduced in the parts of the structures submitted to compression. It could have
543 an impact on the final break of the beam but it is often negligible because the compressive strength is
544 often about ten times higher than the chemical prestress. Furthermore, for prestressed beams, the
545 flexural behaviour explained for reinforced beams is similar: the benefit is improved on the part in
546 tension and the compressive strength is reduced.

547

548

549 **7. Conclusion**

550 The aims of this paper were to show how restraint and stress can modify ASR expansion and to
551 propose a model able to take this effect into account. First, the model was presented. It considers both
552 ASR mechanisms and physical phenomena, such as creep, damage and their coupling, so as to be
553 representative of concrete behaviour. Attention was focused on the gel pressure and on the hardening
554 law chosen to manage the cracking due to ASR. The gel pressure calculation took elastic strains and
555 ASR plastic strains into account in order to respect the principles of poromechanics when representing
556 cracks.

557 The model was calibrated and validated on experimental results [10]. Specimens were tested
558 under several mechanical conditions: creep and shrinkage without ASR, free swelling with or without

559 loads, restrained swelling (with 3 and 5 mm thick steel rings) with or without longitudinal loading.
560 The calculations show numerical results that are realistic when compared to experimentation.

561 Based on this calibration, a theoretical analysis was carried out:

- 562 1. The comparison of expansion under restraint and stresses pointed out the importance of loading
563 chronology in ASR kinetics.
- 564 2. For a final expansion of about 0.3%, a maximum stress of about 3 MPa is reached in the case of
565 expansion that is perfectly restrained in only 1 direction. This seems realistic compared to
566 field experience [26].
- 567 3. For a specimen restrained in three directions, the maximum compressive stress can be expected
568 to be greater and reached about 7 MPa in this work (for a stress free expansion of 0.3%). This
569 result will depend on the capacity of ASR gels to move in the porosity of concrete aggregate,
570 which is taken into account in the gel pressure equation.
- 571 4. Simulated unloading tests during swelling showed that specimens extracted from a structure
572 could crack rapidly due to the relaxing of stress and thus would impact future prognostic tests.
- 573 5. Tension stresses during ASR swelling could lead to premature and greater expansion.

574 Finally, restrained tests were carried out with steel reinforcement (longitudinal ribbed bar and
575 transversal steel rings). They enabled conclusions to be drawn on ASR development in reinforced
576 structures and could help experts in the management of ASR reinforced and damaged structures. The
577 combination of coring direction with cracking anisotropy can lead to differences in the analysis of
578 structures. For a reinforced structure, the stress state can induce anisotropic cracking that leads to weak
579 and strong zones of material which depend on the loading or restraint directions. Basing a prognosis
580 on such tests (residual expansion tests and / or mechanical tests on cores drilled from structures) could
581 thus lead to the structural consequences of ASR being poorly estimated.

582 **REFERENCES**

- 583 [1] E. Bourdarot, A. Sellier, S. Multon, E. Grimal, A review of continuum damage modelling for
584 dam analysis, *European Journal of Environmental and Civil Engineering*. 14 (2010) 805–822.
585 doi:10.1080/19648189.2010.9693263.
- 586 [2] R.G. Charlwood, Predicting the Long Term Behaviour and Service Life of Concrete Dams, in:
587 Graz, Austria, 2009. [http://civil.colorado.edu/~saouma/AAR/Library/Paris-
588 2009/Charlwood/Predicting-long-term.pdf](http://civil.colorado.edu/~saouma/AAR/Library/Paris-2009/Charlwood/Predicting-long-term.pdf) (accessed July 29, 2016).
- 589 [3] R.G. Charlwood, S.V. Solymar, D.D. Curtis, A review of alkali aggregate reactions in
590 hydroelectric plants and dams, in: *Proceedings of the International Conference of Alkali-
591 Aggregate Reactions in Hydroelectric Plants and Dams*, 1992.
- 592 [4] RILEM Technical Comitee 259-ISR, Benchmark/Round Robin Analyses : ASR Prognosis of
593 deterioration and loss of serviceability in structures affected by alkali-silica reactions, (2016).
594 [http://www.rilem.net/global/gene/doc_link.php?doc=2016161048_rilem-tc-259-isr-wg2-
595 benchmark.pdf](http://www.rilem.net/global/gene/doc_link.php?doc=2016161048_rilem-tc-259-isr-wg2-benchmark.pdf) (accessed July 29, 2016).
- 596 [5] N. Baghdadi, F. Toutlemonde, J.-F. Seignol, Modélisation de l’effet des contraintes sur
597 l’anisotropie de l’expansion dans les bétons atteints de réactions de gonflement interne, in:
598 Conférence AUGC, Bordeaux, 2007. [http://www.iut.u-
599 bordeaux1.fr/gc/augc07/index/pdf/BCM/Baghdadi.pdf](http://www.iut.u-bordeaux1.fr/gc/augc07/index/pdf/BCM/Baghdadi.pdf) (accessed May 3, 2016).
- 600 [6] C. Comi, R. Fedele, U. Perego, A chemo-thermo-damage model for the analysis of concrete
601 dams affected by alkali-silica reaction, *Mechanics of Materials*. 41 (2009) 210–230.
602 doi:10.1016/j.mechmat.2008.10.010.
- 603 [7] E. Grimal, A. Sellier, S. Multon, Y. Le Pape, E. Bourdarot, Concrete modelling for expertise of
604 structures affected by alkali aggregate reaction, *Cement and Concrete Research*. 40 (2010)
605 502–507. doi:10.1016/j.cemconres.2009.09.007.
- 606 [8] P. Léger, P. Côté, R. Tinawi, Finite element analysis of concrete swelling due to alkali-
607 aggregate reactions in dams, *Computers & Structures*. 60 (1996) 601–611. doi:10.1016/0045-
608 7949(95)00440-8.
- 609 [9] V. Saouma, L. Perotti, Constitutive model for alkali-aggregate reactions, *ACI Materials
610 Journal*. 103 (2006) 194.
- 611 [10] S. Multon, F. Toutlemonde, Effect of applied stresses on alkali–silica reaction-induced
612 expansions, *Cement and Concrete Research*. 36 (2006) 912–920.
613 doi:10.1016/j.cemconres.2005.11.012.
- 614 [11] E. Grimal, A. Sellier, Y. Le Pape, E. Bourdarot, Creep, Shrinkage, and Anisotropic Damage in
615 Alkali-Aggregate Reaction Swelling Mechanism-Part I. A Constitutive Model, *ACI Materials
616 Journal*. 105 (2008) 227–235.

- 617 [12] A. Sellier, S. Multon, L. Buffo-Lacarrière, T. Vidal, X. Bourbon, G. Camps, Concrete creep
618 modelling for structural applications: non-linearity, multi-axiality, hydration, temperature
619 and drying effects, *Cement and Concrete Research*. 79 (2016) 301–315.
620 doi:10.1016/j.cemconres.2015.10.001.
- 621 [13] M.A. Biot, General Theory of Three-Dimensional Consolidation, *Journal of Applied Physics*. 12
622 (1941) 155–164. doi:10.1063/1.1712886.
- 623 [14] C. Larive, Apports combinés de l'expérimentation et de la modélisation à la compréhension
624 de l'alcali-réaction et de ses effets mécaniques, phdthesis, Ecole Nationale des Ponts et
625 Chaussées, 1997. <https://pastel.archives-ouvertes.fr/tel-00520676/document> (accessed May
626 3, 2016).
- 627 [15] J. Moon, S. Speziale, C. Meral, B. Kalkan, S.M. Clark, P.J.M. Monteiro, Determination of the
628 elastic properties of amorphous materials: Case study of alkali–silica reaction gel, *Cement
629 and Concrete Research*. 54 (2013) 55–60. doi:10.1016/j.cemconres.2013.08.012.
- 630 [16] A. Leemann, P. Lura, E-modulus of the alkali–silica-reaction product determined by micro-
631 indentation, *Construction and Building Materials*. 44 (2013) 221–227.
632 doi:10.1016/j.conbuildmat.2013.03.018.
- 633 [17] T. Adachi, S. Sakka, Dependence of the elastic moduli of porous silica gel prepared by the sol-
634 gel method on heat-treatment, *J Mater Sci*. 25 (1990) 4732–4737. doi:10.1007/BF01129933.
- 635 [18] Z. Bažant, G. Zi, C. Meyer, Fracture Mechanics of ASR in Concretes with Waste Glass Particles
636 of Different Sizes, *Journal of Engineering Mechanics*. 126 (2000) 226–232.
637 doi:10.1061/(ASCE)0733-9399(2000)126:3(226).
- 638 [19] C.F. Dunant, K.L. Scrivener, Effects of uniaxial stress on alkali–silica reaction induced
639 expansion of concrete, *Cement and Concrete Research*. 42 (2012) 567–576.
640 doi:10.1016/j.cemconres.2011.12.004.
- 641 [20] S. Multon, F. Toutlemonde, Effect of moisture conditions and transfers on alkali silica
642 reaction damaged structures, *Cement and Concrete Research*. 40 (2010) 924–934.
643 doi:10.1016/j.cemconres.2010.01.011.
- 644 [21] H. Kagimoto, Y. Yasuda, M. Kawamura, ASR expansion, expansive pressure and cracking in
645 concrete prisms under various degrees of restraint, *Cement and Concrete Research*. 59
646 (2014) 1–15. doi:10.1016/j.cemconres.2014.01.018.
- 647 [22] B. Capra, A. Sellier, Anisotropic modelling of alkali–aggregate reaction in concrete, in: *Quebec
648 City, 2000*: pp. 929–938.
- 649 [23] A. Sellier, B. Bary, Coupled damage tensors and weakest link theory for the description of
650 crack induced anisotropy in concrete, *Engineering Fracture Mechanics*. 69 (2002) 1925–1939.
651 doi:10.1016/S0013-7944(02)00069-3.

- 652 [24] L.F.M. Sanchez, S. Multon, A. Sellier, M. Cyr, B. Fournier, M. Jolin, Comparative study of a
653 chemo–mechanical modeling for alkali silica reaction (ASR) with experimental evidences,
654 Construction and Building Materials. 72 (2014) 301–315.
655 doi:10.1016/j.conbuildmat.2014.09.007.
- 656 [25] M.T. Van Genuchten, A Closed-form Equation for Predicting the Hydraulic Conductivity of
657 Unsaturated Soils¹, Soil Science Society of America Journal. 44 (1980) 892.
658 doi:10.2136/sssaj1980.03615995004400050002x.
- 659 [26] P. Rivard, G. Ballivy, C. Gravel, F. Saint-Pierre, Monitoring of an hydraulic structure affected
660 by ASR: A case study, Cement and Concrete Research. 40 (2010) 676–680.
661 doi:10.1016/j.cemconres.2009.09.010.
- 662 [27] M. Alnaggar, G. Cusatis, G.D. Luzio, Lattice Discrete Particle Modeling (LDPM) of Alkali Silica
663 Reaction (ASR) deterioration of concrete structures, Cement and Concrete Composites. 41
664 (2013) 45–59. doi:10.1016/j.cemconcomp.2013.04.015.
- 665 [28] P. Rivard, F. Saint-Pierre, Assessing alkali-silica reaction damage to concrete with non-
666 destructive methods: From the lab to the field, Construction and Building Materials. 23
667 (2009) 902–909. doi:10.1016/j.conbuildmat.2008.04.013.
- 668 [29] P.S. Chana, BOND STRENGTH OF REINFORCEMENT IN CONCRETE AFFECTED BY ALKALI SILICA
669 REACTION, TRRL CONTRACTOR REPORT. (1989). <https://trid.trb.org/view.aspx?id=314058>
670 (accessed July 29, 2016).
- 671 [30] P.S. Chana, G.A. Korobokis, THE STRUCTURAL PERFORMANCE OF REINFORCED CONCRETE
672 AFFECTED BY ALKALI SILICA REACTION: PHASE II, (1992).
673 <https://trid.trb.org/view.aspx?id=369872> (accessed July 29, 2016).
- 674 [31] S.R. Rigden, Y. Majlesi, E. Burley, BOND STRESS FAILURE IN ALKALI SILICA REACTIVE
675 REINFORCED CONCRETE BEAMS, in: 1992. <https://trid.trb.org/view.aspx?id=450549>
676 (accessed July 29, 2016).
- 677 [32] F. Habibi, S.A. Sheikh, N. Orbovic, D.K. Panesar, F.J. Vecchio, ALKALI AGGREGATE REACTION
678 IN NUCLEAR CONCRETE STRUCTURES: PART 3: STRUCTURAL SHEAR WALL ELEMENTS, in:
679 Manchester, UK, 2015.
- 680 [33] S. Multon, J.-F. Seignol, E. Bourdarot, A. Jeanpierre, F. Toutlemonde, Effets structuraux de
681 l’alcali-réaction: Apports d’une expérimentation sur éléments de structures à la validation de
682 modèles, Revue Européenne de Génie Civil. 9 (2005) 1219–1247.
683 doi:10.1080/17747120.2005.9692808.
- 684